AI-ENHANCED E-NOSE BASED ON FILM BULK ACOUSTIC RESONATORS FOR IDENTIFICATION OF VOLATILE ORGANIC COMPOUNDS

Luwei Wang[1], Mengyao Xiao[1], Weixin Liu[1], Dongxiao Li[1], Yingpeng Wang[1], Ying Zhang[2], Yao Zhu[2], and Chengkuo Lee[1]

[1]Department of Electrical & Computer Engineering, National University of Singapore, SINGAPORE

and

[2]Institute of Microelectronics (IME), Agency for Science Technology, and Research (A*STAR), SINGAPORE

2026 IEEE 39th International Conference on Micro Electro Mechanical Systems (MEMS) | 979-8-3315-7251-8/26/$31.00 ©2026 IEEE | DOI: 10.1109/MEMS64181.2026.11419558

ABSTRACT

Real-time detection of volatile organic compounds (VOCs) is critical for various applications such as environmental monitoring, disease diagnosis, and smart farming, driving the rapid development of electronic-nose (e-nose) technologies. Microelectromechanical systems (MEMS) enable miniaturized VOC sensing, among which film bulk acoustic resonators (FBARs) stand out for their superior sensitivity derived from ultrahigh resonant frequencies. Here, we propose an artificial intelligence (AI)-enabled e-nose based on a graphene oxide (GO) functionalized FBAR to realize various VOC detection. Leveraging the machine learning data analytics, our system achieves 100% accuracy in classifying three VOCs. In addition to frequency shift, time-domain responses during adsorption and desorption yield are incorporated for capturing richer dynamic fingerprints, enabling accurate identification and concentration prediction of VOC mixtures.

KEYWORDS

Electronic-nose, film bulk acoustic resonator, volatile organic compounds mixtures detection, machine learning

INTRODUCTION

VOC detection plays an important role in agricultural safety, industrial environments, and disease monitoring [1], [2]. Over the past decade, VOC sensors based on different working mechanisms have been developed [3]. Most existing systems focus either on identifying a single VOC or recognizing different mixing ratios of VOC mixtures. However, identifying and predicting the concentrations within VOC mixtures remains a great challenge [4].

MEMS-based VOC sensors based on cantilevers [5], quartz crystal microbalances (QCMs) [6], surface acoustic wave (SAW) [7], and film bulk acoustic resonators (FBARs) have attracted growing attention due to their ability to detect minute variations in surface mass loading [8]. Among them, FBARs, with their high resonant frequencies in the gigahertz range, excellent integrability, and microscale footprint, represent a highly promising platform for VOC sensing [9], [10], [11].

Most existing VOC sensing systems employ sensor arrays coated with different sensing materials to achieve multi-gas detection [12], [13], but this strategy increases fabrication complexity and circuit integration challenges. Temperature-modulated sensing offers an alternative route to diversify sensing responses [14], [15]. However, this approach may also introduce fabrication complexity and have some limitations in practical use. By integrating machine learning [16], it becomes possible to achieve multi-VOC detection at room temperature using a single sensing material [17]. Current systems predominantly use frequency-domain features for training the machine learning model, such as resonant frequency shifts and S_{11} variations. However, quantitative prediction also remains challenging. Recently, time-domain features capturing adsorption–desorption dynamics have also gained increasing interest, providing a pathway toward more comprehensive VOC mixture analysis.

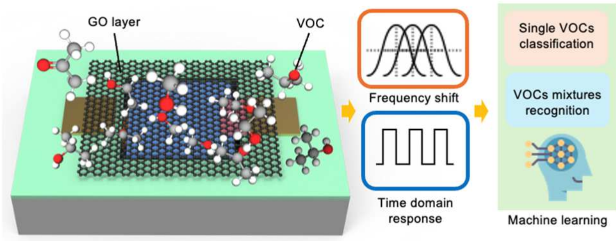

Figure 1: Schematic diagram of the AI-enhanced e-nose based on FBAR for identification of VOCs.

In this work, we reported an AI-enhanced e-nose based on a scandium-doped aluminum nitride (ScAlN) FBAR (Fig. 1). A GO sensing layer was deposited on the FBAR to provide abundant surface sites for VOCs adsorption and to capture VOC fingerprints with high sensitivity. Distinct frequency-domain responses allow accurate classification of single VOCs, including ethanol (ETH), isopropyl alcohol (IPA), and methanol (MTH). In addition to frequency-domain responses, time-domain responses are also extracted to characterize the adsorption and desorption dynamics of VOC mixtures. Leveraging these fingerprints and with the aid of machine learning, our system achieves VOC mixtures identification with an accuracy of 89.16%. Furthermore, quantitative prediction of VOC mixtures reaches accuracies of 85.22%, 84.46%, and 97.14% for the mixtures of ETH: IPA, ETH: MTH, and IPA: MTH, respectively, each evaluated across 15 concentration combinations (i.e., 6 ppm: 19 ppm, 8.5 ppm: 16.5 ppm, 12.5 ppm: 12.5 ppm, 12.5 ppm: 37.5 ppm, 15 ppm: 45 ppm, 16.5 ppm: 8.5 ppm, 16.5 ppm: 33 ppm, 19 ppm: 6 ppm, 20 ppm: 40 ppm, 25 ppm: 25 ppm, 30 ppm: 30 ppm, 33 ppm: 16.5 ppm, 37.5 ppm: 12.5 ppm, 40 ppm: 20 ppm, and 45 ppm: 15 ppm). These combinations span mixing ratios of 1: 1, 1: 2, 1: 3, 2: 1, and 3: 1 across total concentration levels of 25 ppm, 50 ppm, and 60 ppm, providing a comprehensive evaluation of the capability of the AI-enhanced e-nose to quantify VOC mixtures under diverse concentration regimes.

DESIGN AND CHARACTERIZATION

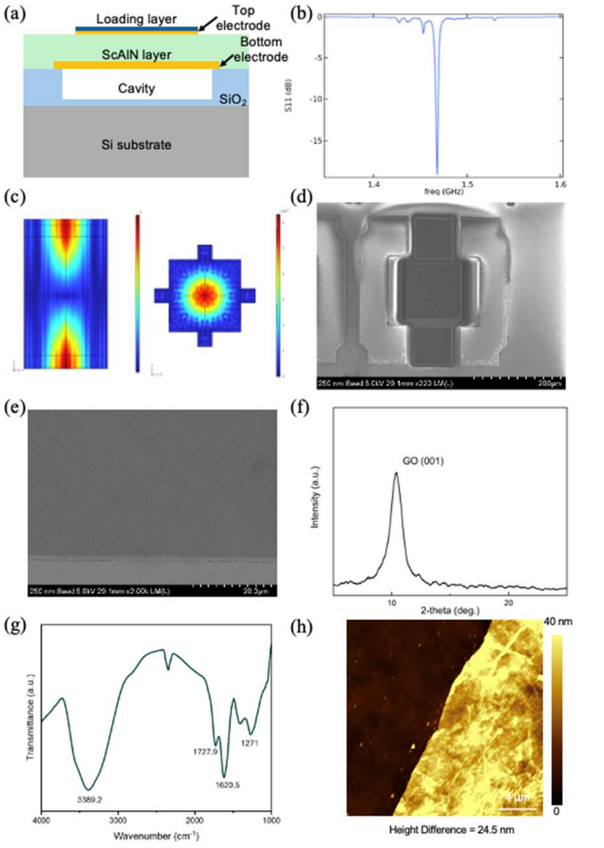

Figure 2: (a) Cross-sectional view of FBAR. (b) Simulation results of response curve scattering parameter S11 versus frequency. (c) Vibration mode shape obtained from the FEM simulation. The surface displacement amplitude is shown in both the top view and cross-sectional view at the eigenfrequency. (d) SEM image of the FBAR before GO coated. (e) SEM Image of the FBAR after GO coated. (f) XRD analysis of GO film. (g) FTIR spectrum of the GO film. (h) AFM images of GO film.

The cross-sectional view of the FBAR is illustrated in Fig. 2a, which consists of top and bottom metal electrodes, and a ScAlN (15% Sc) piezoelectric thin film. The membrane is suspended above an air cavity within the silicon dioxide (SiO_2) layer, forming a square active region for acoustic resonance. When a radio-frequency (RF) signal is applied across the electrodes, the ScAlN layer generates high-frequency acoustic waves, which are confined within the membrane by the underlying cavity through constructive reflection. Finite element (FEM) simulation indicates a resonant frequency of ~1.47 GHz (Fig. 2b), and the corresponding surface displacement amplitude is shown in Fig. 2c, which reveals a higher amplitude concentration at the center of the device. The scanning electron microscopy (SEM) image of the fabricated FBAR is shown in Fig. 2d. After GO film deposition, the surface morphology (Fig. 2e) reveals a characteristic wrinkled texture. The structural characteristics of the GO film are verified by X-ray diffraction (XRD), which exhibits the characteristic GO (001) peak (Fig. 2f). Fourier transform infrared spectroscopy (FTIR) indicates the presence of rich functional groups in GO (Fig. 2g) that serve as active adsorption sites. Atomic force microscopy (AFM) further reveals the surface topology and roughness of the GO film and indicates an average thickness of ~24.5 nm (Fig. 2h).

RESULTS AND DISCUSSIONS

AI Analysis of Single VOCs

With the GO-functionalized FBAR, the device is exposed to three different VOCs: ETH, IPA, and MTH. Fig. 3a–c presents the S_{11}-frequency responses for ETH (Fig. 3a), IPA (Fig. 3b), and MTH (Fig. 3c). As the concentration of each VOC increases, the resonant frequency gradually decreases, which is primarily attributed to the mass-loading effect caused by VOC adsorption on the GO sensing layer. To further quantify the correlation between VOC concentration and frequency response, the extracted resonant-frequency shifts (Δf) are plotted against concentration in Fig. 3d. All three VOCs exhibit a clear monotonic trend, where higher concentrations lead to larger negative frequency shifts. Among them, ETH induces the largest frequency shift, followed by IPA and MTH, indicating the different interaction strengths between each VOC and the GO film. This concentration-dependent behavior confirms the capability of the GO-functionalized FBAR to serve as a sensitive and discriminative platform for VOC detection.

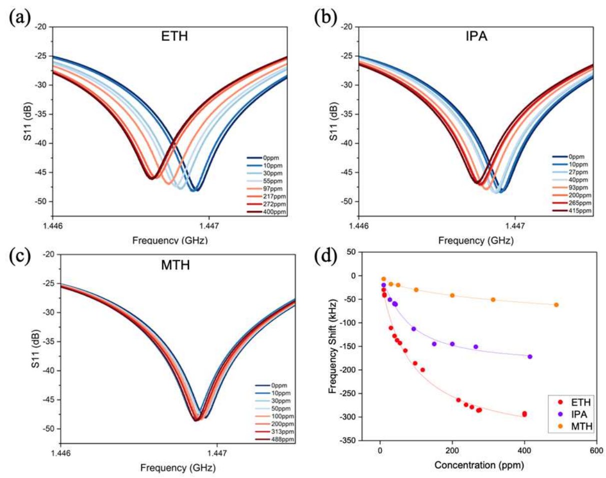

Figure 3: (a)-(c) The static characterizations for three VOCs: (a) ETH, (b) IPA, (c) MTH. (d) Sensing response under different VOCs with various concentrations.

Figure 4a shows the real-time response of the e-nose under 10 cyclic exposures, consisting of 4 min N_2 purging followed by 4 min exposure to 20 ppm ETH, exhibiting high repeatability and stable frequency shifts across all cycles. The principal component analysis (PCA) distribution of the three VOCs (ETH, IPA, and MTH) is shown in Fig. 4b, where the samples form separated clusters in the reduced feature space. By applying a support vector machine (SVM) classifier to the extracted features of frequency-domain responses, classification of the three single VOCs is achieved, with the accuracy of 100%.

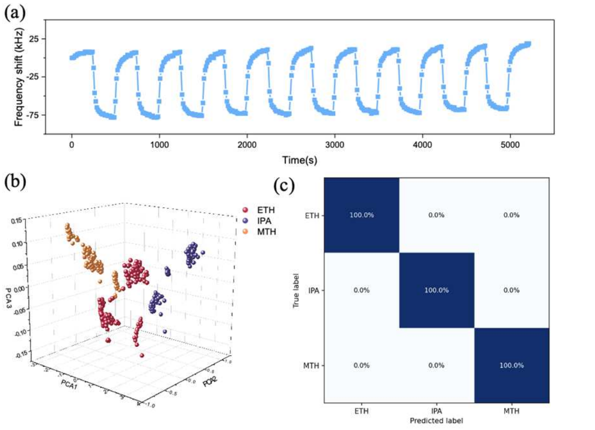

Figure 4: (a) Real-time response to 20 ppm ETH under cyclic exposure, showing good repeatability. (b) The identification of VOCs by PCA plots in 3-dimension. (c) The confusion matrices for VOCs classification base on SVM.

Real-time Response and VOC Mixtures Detection

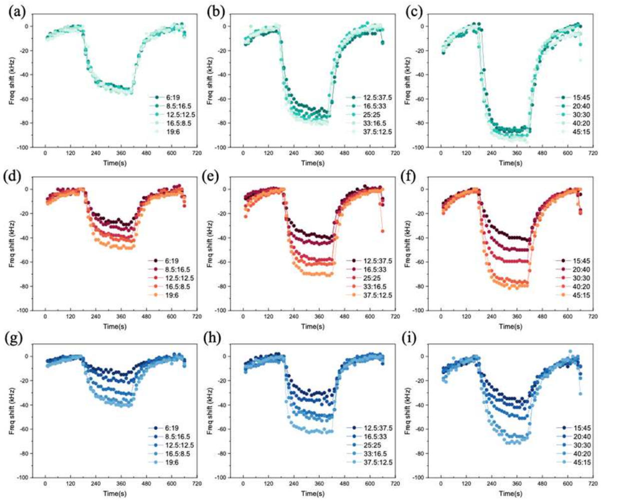

Figure 5: Time-domain responses for VOC mixtures with different mixing concentrations. (a)-(c) ETH: IPA, (d)-(f) ETH: MTH, (g)-(i) IPA: MTH.

The capability of the e-nose to discriminate VOC mixtures was evaluated by testing three binary VOC combinations: ETH: IPA (Fig. 5a-5c), ETH: MTH (Fig. 5d-5f), and IPA: MTH (Fig. 5g-5i). Each mixture set consisted of 15 concentration pairs spanning mixing ratios of 1:1, 1:2, 2:1, 1:3, and 3:1 across three total-concentration levels: 25 ppm (Fig. 5a, Fig. 5d, Fig. 5g), 50 ppm (Fig. 5b, Fig. 5e, Fig. 5h), and 60 ppm (Fig. 5c, Fig. 5f, Fig. 5i). The broad range of combinations aims to assess the capability of the proposed e-nose to discriminate VOC mixtures across diverse mixing ratios and concentration levels. For each VOC pair, the sensor was sequentially exposed to N_2, the VOC mixture, and N_2 again with identical timing intervals to ensure consistent adsorption-desorption cycles. The total gas flow rate was kept the same as that used for single-VOC measurements. For ETH: IPA mixtures (Fig. 5a-5c), the real-time responses corresponding to different mixing ratios appear highly similar within each total-concentration level. Consequently, distinguishing different ETH: IPA compositions based on the frequency shift is challenging. For ETH: MTH mixtures (Fig. 5d-5f), real-time responses show more noticeable variations among the mixing ratios. Mixtures containing higher concentrations of ETH result in larger downward frequency shifts and slightly faster adsorption kinetics. For IPA: MTH mixtures, similar behavior is observed. As the proportion of IPA increases, the response curves show deeper frequency shifts and faster adsorption. Since certain mixtures show overlapping frequency-shift behaviors, frequency-domain information alone is insufficient for precise identification. Incorporating time-domain dynamics together with machine-learning models allows the extraction of more features, enabling reliable recognition and quantification of VOC mixtures.

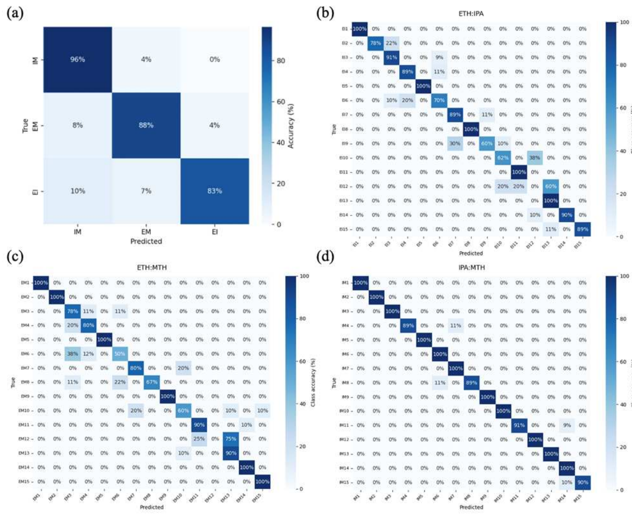

Figure 6: (a) Confusion matrix for different VOC mixtures. (b) Confusion matrix for ETH: IPA mixtures at different concentrations. (c) Confusion matrix for ETH: MTH mixtures at different concentrations. (d) Confusion matrix for IPA: MTH mixtures at different concentrations.

The developed SVM classifier was employed to analyze the extracted features. Each sample consists of 55 data points collected during one full sensing cycle, including exposure to N_2, the VOC mixture, and N_2. The entire dataset was randomly divided into training and testing sets using an 8:2 split. As shown in Fig. 6a, the classification of the three VOC mixture types (ETH: IPA, ETH: MTH, and IPA: MTH) achieves an overall accuracy of 89.16%. Beyond identifying mixture types, the SVM model was further applied to quantitative estimation of mixture compositions across 15 concentration combinations for each VOC pair. The corresponding confusion matrices for ETH: IPA, ETH: MTH, and IPA: MTH mixtures are achieved with the accuracies of 85.22% (Fig. 6b), 84.46% (Fig. 6c), and 97.14% (Fig. 6d), respectively. The AI-enhanced e-nose demonstrates the capability of resolving VOC mixtures across different concentration levels. Mixtures with identical mixing ratios but different total concentrations can be distinguished. These results highlight that combining time-domain response dynamics with machine-learning algorithms allows the FBAR-based e-nose to achieve reliable classification and quantitative analysis of VOC mixtures, showcasing the great potential of the AI-enhanced e-nose for wide applications, including environmental monitoring, industrial safety, and indoor air quality assessment.

CONCLUSIONS

In this work, we developed an AI-enhanced e-nose based on a GO-functionalized FBAR for VOCs detection and quantitative mixture analysis. By constructing features from frequency-domain responses, single-VOC classification achieved 100% accuracy. The proposed machine learning approach incorporates time-domain adsorption–desorption dynamics as additional features to further realize VOC mixtures recognition with an accuracy of 89.6% and quantitative prediction accuracies of 85.22%, 84.46%, and 97.14% for ETH: IPA, ETH: MTH, and IPA: MTH mixtures, respectively. Overall, the proposed GO-functionalized FBAR shows great potential as an e-nose for VOC mixtures detection in widespread applications of environmental monitoring, disease diagnosis, and smart farming.

ACKNOWLEDGEMENTS

This research was supported by the RIE Advanced Manufacturing and Engineering (AME) Programmatic Grant (A18A4b0055), RIE 2025-Industry Alignment Fund-Industry Collaboration Projects (IAF-ICP) (Grant I2301E0027), National Research Foundation Competitive Research Programme (NRF-CRP28-2022-0002), Research Platform for Biomedical and Health Technology (RP-BTH-Prof. LEE Chengkuo) in NUS (Suzhou) Research Institute.

REFERENCES

[1] Z. Luo, D. Li, X. Le, *et al.*, "Ultra-Compact and High-Performance Suspended Aluminum Scandium Nitride Lamb Wave Humidity Sensor with Graphene Oxide Layer" *Nanoscale*, vol. 16, pp. 10230–10238, 2024.

[2] J. Zhou, X. Liu, H. Zhou, *et al.*, "Artificial-Intelligence-Enhanced Mid-infrared Lab-on-a-Chip for Mixture Spectroscopy Analysis," *Laser Photon. Rev.*, vol. 19, pp. 2400754, 2025.

[3] X. Liu, Z. Zhang, J. Zhou, W. Liu, G. Zhou, and C. Lee, "Artificial Intelligence-Enhanced Waveguide 'Photonic Nose'- Augmented Sensing Platform for VOC Gases in Mid-Infrared," *Small*, vol. 20, 2024.

[4] W. Liu, Y. Ma, X. Liu, *et al.*, "Larger-Than-Unity External Optical Field Confinement Enabled by Metamaterial-Assisted Comb Waveguide for Ultrasensitive Long-Wave Infrared Gas Spectroscopy," *Nano Lett.*, vol. 22, pp. 6112-6120, 2022.

[5] D. Li, B. Zhu, K. Pang, *et al.*, "Virtual Sensor Array Based on Piezoelectric Cantilever Resonator for Identi fi cation of Volatile Organic Compounds," *ACS Sensors*, vol. 7, pp. 1555-1563, 2022.

[6] D. Li, Z. Xie, M. Qu, Q. Zhang, Y. Fu, and J. Xie, "Virtual Sensor Array Based on Butterworth-Van Dyke Equivalent Model of QCM for Selective Detection of Volatile Organic Compounds," *ACS Appl. Mater. Interfaces*, vol. 13, pp. 47043–47051, 2021.

[7] T. Wang, X. Mu, A. B. Randles, Y. Gu, and C. Lee, "Diaphragm Shape Effect on the Sensitivity of Surface Acoustic Wave based Pressure Sensor for Harsh Environment," *Appl. Phys. Lett.*, vol. 107, pp. 123501, 2015.

[8] H. Zhao, S. Fan, Y. Chen, *et al.*, "Oxygen Plasma-Treated Graphene Oxide Surface Functionalization for Sensitivity Enhancement of Thin-Film Piezoelectric Acoustic Gas Sensors," *ACS Appl. Mater. Interfaces*, vol. 9, pp. 40774-40781, 2017.

[9] X. Wang, C. Liu, Y. Zhang, *et al.*, "Thin $Sc_{0.2}Al_{0.8}N$ Film Based 15 GHz Wideband Filter : Towards mmWave Acoustic Filters," *2023 Int. Electron Devices Meet.*, pp. 1-4, 2023.

[10] Y. Zhang, W. Yang, C. Liu, X. Wang, E. W. Y. Zhun, and N. Wang, "Experimental and Numerical Study on the Second Order Harmonic (H_2) and Third Order Intermodulation Distortion (IMD_3) Response of Scandium Aluminum Nitride Based FBAR Devices with Different Scandium Doping Levels," *2022 IEEE Int. Ultrason. Symp.*, pp. 1-3, 2025.

[11] C. Liu, X. Wang, W. Yang, Y. Zhang, and euguene yi zhu Woo, "A $Sc_{0.2}Al_{0.8}N$-based 14 GHz Film Bulk Acoustic Resonator with over 8% Coupling Coefficient and over 400 Quality factor for Ku-band applications," *2023 IEEE Int. Ultrason. Symp.*, pp. 1-4, 2023.

[12] X. Wang, X. Kang, X. Chen, *et al.*, "Pocket Electronic Nose Integrating an Ultra-Compact Sensor Array Chip and Spatiotemporal Network Enables Highly Selective Gas Sensing," *ACS Sensors*, vol. 10, pp. 6887-6896, 2025.

[13] Z. Wang, Z. Zhao, S. Jin, *et al.*, "Investigation Of Sorptive Interactions between Volatile Organic Compounds And Supramolecules at Dynamic Oscillation using Bulk Acoustic Wave Resonator Virtual Sensor Arrays," *Microsystems Nanoeng.*, vol. 10, pp. 99, 2024.

[14] H. Mei, J. Peng, T. Wang, *et al.*, "Smart Vocs Recognition System based on Single Gas Sensor and Multi-Task Deep Learning Model," *Sensors Actuators B. Chem.*, vol. 439, pp. 137853, 2025.

[15] M. Xiao, A. Xu, Z. Sui, *et al.*, "Multifucnrional MEMS, NEMS Micro/Nano-Structures Enabled by Piezoelectric and Ferroelectric Effects," *Nanoscale Horizons*, vol. 10, pp. 137853, 2025.

[16] W. Luo, F. Dai, Y. Liu, X. Wang, and M. Li, "Pulse-Driven MEMS Gas Sensor combined with Machine Learning for Selective Gas Identification," *Microsystems Nanoeng.*, vol. 11, pp. 2744-2771, 2025.

[17] Z. Zhang, L. Wang, and C. Lee, "Recent Advances in Artificial Intelligence Sensors," *Adv. Sens. Res.*, vol. 2, pp. 2200072, 2023.

CONTACT

* C. Lee, elelc@nus.edu.sg